J. Fluid Mech. (2013), *vol.* 726, R3, doi:10.1017/jfm.2013.261

JFM RAPIDS
journals.cambridge.org/rapids

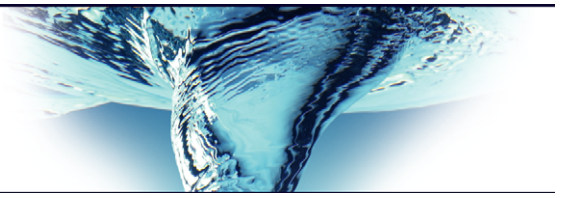

Air entrainment during impact of droplets on liquid surfaces

Tuan Tran[1,†], Hélène de Maleprade[2], Chao Sun[1,†] and Detlef Lohse[1,†]

[1]Physics of Fluids Group, Faculty of Science and Technology, University of Twente, 7500 AE Enschede, The Netherlands
[2]Département de Mécanique, École Polytechnique, 91128 Palaiseau Cedex, France

(Received 18 March 2013; revised 18 March 2013; accepted 20 May 2013; first published online 6 June 2013)

We study drop impact on a deep pool of the same fluid, with an emphasis on the air layer trapped under the droplets from its formation to its rupture. The penetration velocity of the air layer at a very short time scale prior to its rupture is shown, using an energy argument and experimental verification, to be one-half of the impact velocity. We then deduce the dependence of the rupture position on the liquid viscosity and the impact velocity. We show that the volume of the resulting air bubbles can be related to both those resulting from droplets impacting on solid surfaces and those resulting from rigid spheres impacting on liquid surfaces.

Key words: breakup/coalescence, drops and bubbles, thin films

1. Introduction

More than a hundred years after Worthington (1908) started to study droplet impact phenomena, the subject continues to attract researchers of various disciplines, not only because of many fundamental questions originating from the phenomena involved, but also because of its importance in a wide range of technological applications, as reviewed by Prosperetti & Oguz (1993), Weiss & Yarin (1999) and Yarin (2006). The emphasis has been on bubble entrapment, bouncing, splashing, crown formation and droplet atomization. In the case of droplets impacting on liquid surfaces, of particular interest is the entrapment of an air layer, which may rupture and lead to the entrainment of either a multitude of tiny bubbles (Mesler entrainment; see e.g. Esmailizadeh & Mesler 1986; Pumphrey & Elmore 1990) or only a few individual bubbles (see Thoroddsen, Etoh & Takehara 2003; Thoroddsen *et al.* 2012). Note that these bubble entrapment processes take place at very small time scales after impact, as opposed to that due to the collapse of the impact crater, which happens at much longer

† Email addresses for correspondence: t.tran@utwente.nl, c.sun@utwente.nl, d.lohse@utwente.nl

© Cambridge University Press 2013

https://doi.org/10.1017/jfm.2013.261 Published online by Cambridge University Press

Liquid	Viscosity, ν_l (cSt)	Density, ρ (kg m^{-3})	Surface tension, σ (N m^{-1})	$Re = RV/\nu_l$	$We = \rho RV^2/\sigma$
5 cSt silicone oil	5	916	0.0197	96–177	11–37
10 cSt silicone oil	10	934	0.0201	50–180	12–158
20 cSt silicone oil	20	953	0.0208	24–106	11–217

TABLE 1. Properties of the silicone fluids used in the experiments and the corresponding ranges of the Reynolds number and the Weber number.

time scales (see Pumphrey, Crum & Bjørnø 1989; Rein 1993). These findings, together with the one reported by Xu, Zhang & Nagel (2005) that splashing can be completely suppressed by reducing the ambient pressure, illustrate the complexity of the impact dynamics at early time scales and highlight the role of the air layer between the drop and the surface – for some recent investigations of the air layer, see, for example, Thoroddsen *et al.* (2005), Mandre, Mani & Brenner (2009), Mani, Mandre & Brenner (2010), Hicks & Purvis (2010, 2011), Duchemin & Josserand (2011), Bouwhuis *et al.* (2012), Hicks *et al.* (2012), Kolinski *et al.* (2012), Lee *et al.* (2012), Mandre & Brenner (2012), Tran *et al.* (2012), van der Veen *et al.* (2012) and Liu, Tan & Xu (2013).

The goal of this study is to focus on the dynamics of droplets impacting on a deep liquid pool of the same liquid, in particular the very beginning of the process when the two liquid surfaces start being deformed due to the pressure build-up. This deformation entrains an air layer into the pool, which later ruptures to create air bubbles. We investigate the penetration velocity and thinning of the air film under the drop. We also study the rupture process, and the resulting entrapped air bubbles, and relate the volume of the entrapped air to that in the case of liquid droplets impacting on solid surfaces and in the case of solid spheres impacting on liquid surfaces.

2. Experimental details

In figure 1(*a*), we show a schematic of our experimental set-up used to study the impact of droplets on a liquid pool. The thickness of the pool is roughly 10 mm, which can be considered as the deep pool limit. Droplets of uniform size (radius $R \approx 0.95$ mm) are generated by pushing liquid out of a fine needle (24-gauge stainless-steel needle, Hamilton Co.) at a low rate ($\approx$0.05 ml min^{-1}). A droplet falls under its own weight onto a pool of the same liquid. The impact velocity V of the drop is varied between 0.3 and 2.3 m s^{-1} by adjusting the needle's height. Both the drop radius R and velocity V in each experiment are measured before the impact time by a high-speed camera (Photron 1024 PCI) from the side. The working liquid in our experiments are silicone oils with viscosity $\nu_l = 5,\ 10$ and 20 cSt. We choose silicone oils as working fluids because it has been shown by Saylor & Bounds (2012) that the process of formation and subsequent rupture of the air layer is more repeatable for silicone oils than for water. The exact properties of these fluids are listed in table 1.

We record the impacting process from the side and the bottom by two synchronous high-speed cameras (Photron SA1.1 and SA2 for the side- and bottom-view recordings, respectively) with frame rates up to 40 000 frames per second. The side-view camera (camera S in figure 1*a*) is slightly tilted upwards (with an angle $\approx 2^\circ$) to look at the impacting point from underneath the liquid. We use a long working distance

https://doi.org/10.1017/jfm.2013.261 Published online by Cambridge University Press

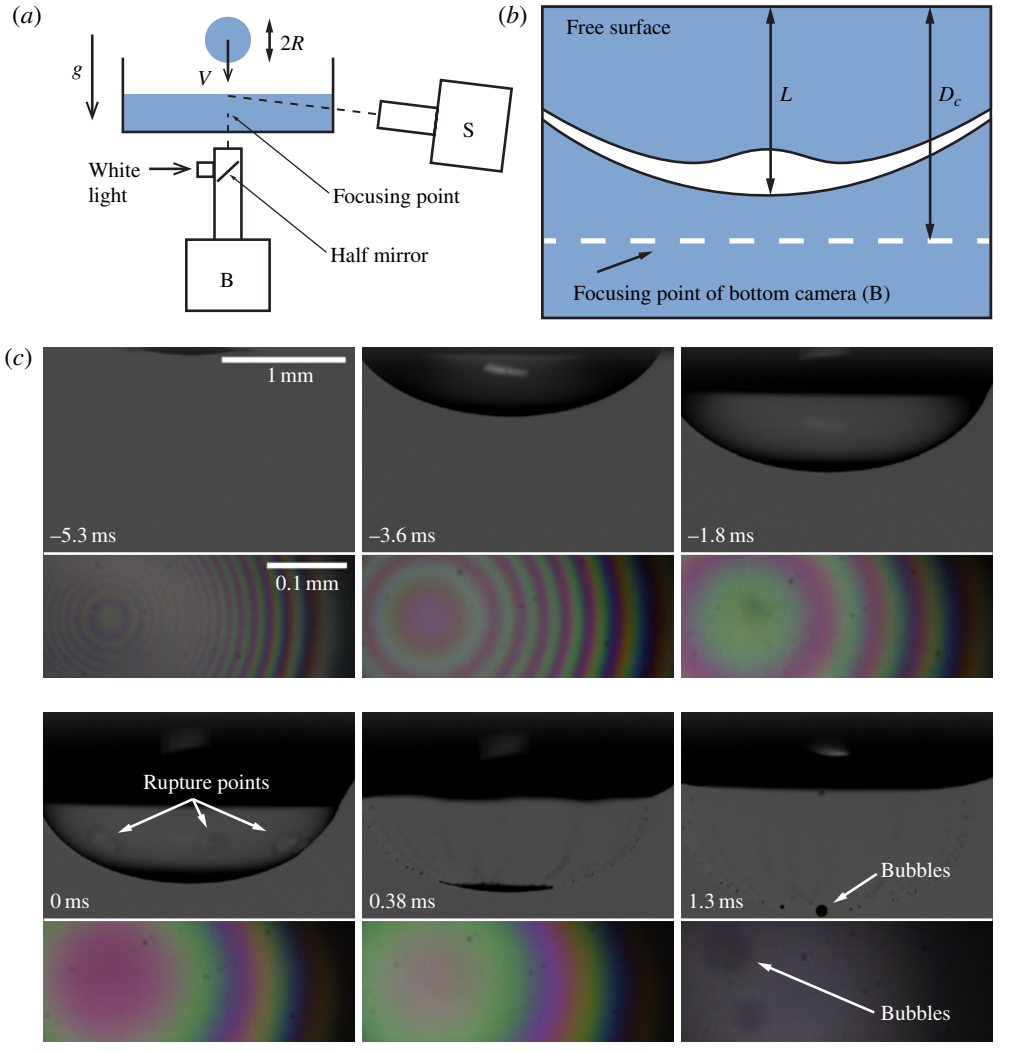

FIGURE 1. (*a*) Schematic (not to scale) of the experimental set-up used to observe the impact of droplets on a deep pool of the same liquid. (*b*) Schematic (not to scale) of the air film layer as the drop penetrates into the pool. The distance between the initial surface of the pool and the bottom of the air film is denoted L. The bottom camera is focused at a distance D_c under the free surface of the pool. When the air film passes the focusing point of the camera ($L = D_c$), the bottom camera records interference fringes caused by light reflected from the two surfaces of the air film. (*c*) Series of representative images recorded from the side-view and bottom-view cameras.

microscope (Navitar 12× UltraZoom) and a 1.5× objective to obtain an optical resolution 4.2 μm.

In figure 1(*c*), we show a series of representative images of the impact taken from the side and from the bottom. We take the reference time ($t = 0$) as the time at which the film rupture is first detected from the side-view recording (see figure 1*c*). The deformation of the pool surface is due to the air pressure build-up between the pool and the drop (see figure 1*b*), and takes the shape of a growing spherical cap, as shown

https://doi.org/10.1017/jfm.2013.261 Published online by Cambridge University Press

in the subsequent images of figure 1(*c*). The observation of the deformation of the pool surface is possible because of the presence of a thin air layer trapped between the pool and the drop. At relatively low impact velocity (i.e. smaller than 0.5, 0.6 and 0.75 m s^{-1} for 5, 10, 20 cSt droplets, respectively), this air layer inhibits coalescence of the droplet and the surface, and eventually causes the droplet to bounce off (see Thoroddsen *et al.* (2012) for the conditions for bouncing in a larger viscosity range). Increasing the impact velocity causes rupture of this air layer, either at isolated points or simultaneously along a horizontal ring. In the side views of figure 1(*c*), after the rupture time ($t = 0$ ms), the ruptured holes expand due to surface tension, leaving small air bubbles behind the receding edges. The expanding velocity of the ruptured holes, as well as the formation and the total volume of these small bubbles, have been discussed in detail by Thoroddsen *et al.* (2012). After the film rupture, which leads to the coalescence of the drop and the liquid pool, the liquid in the drop penetrates even deeper into the pool, creating a crater. The dynamics of this crater (size, growing velocity, horizontal and vertical expansions) was considered both theoretically and experimentally by Engel (1967), Bisighini *et al.* (2010) and Deng, Anilkumar & Wang (2010).

The bottom-view camera (camera B in figure 1*a*) is connected to a long working distance microscope (Navitar 12× UltraZoom) and a 10× objective to observe the bottom of the air film. The field of view and the optical resolution obtained with this system are 1 mm and 1.2 μm, respectively. White illumination light from a high-intensity light source (Olympus ILP-1) is supplied through a coaxial port of the microscope. The focus point of the objective is at a distance D_c under the surface of the pool (see figure 1*b*); D_c can be varied between 0 and 3 mm. As the drop penetrates into the liquid pool, the air film trapped between the drop and the pool surface moves down and passes this focusing point. At that moment, the illumination light is reflected from both surfaces of the air film back to the camera. The resulting images are rings of rainbow colours shown in the bottom views of figure 1(*c*). By repeating the experiment with the same impact velocity while changing the focusing position of the objective, we obtain the interference fringes at different vertical points of the impact process. This makes it possible to examine the evolution of the film thickness profile as the film moves into the pool. The method used to extract the absolute thickness of the air film is based on colour interferometry and has been reported earlier by Bouwhuis *et al.* (2012) and van der Veen *et al.* (2012).

3. Results and discussion

3.1. *Penetration velocity before air film rupture*

In figure 2(*a*), we show the penetration depth L, the distance between the pool's initial surface and the bottom of the air film (figure 1*b*), normalized by the drop radius R, as a function of time. The penetration depth was measured for impact of droplets having the same velocity but different viscosities. Each curve starts from the impact time, defined as the time at which the deformation of the pool surface is first detected from the side-view recording, and ends at the rupture time. It is evident that, although increasing viscosity (from 5 to 20 cSt) delays the rupture time, the penetration depth increases linearly in time with an almost identical rate. However, as seen from figure 2(*b*), the penetration velocity V_p, defined as the averaged velocity of the bottom of the air film before its rupture, does not depend on viscosity. In figure 2(*b*), we show the normalized penetration velocity V_p/V for various impact velocities (0.3 m $s^{-1} < V <$ 1.2 m s^{-1}) and viscosities ($\nu_l = 5,\ 10,\ 20$ cSt). Indeed,

https://doi.org/10.1017/jfm.2013.261 Published online by Cambridge University Press

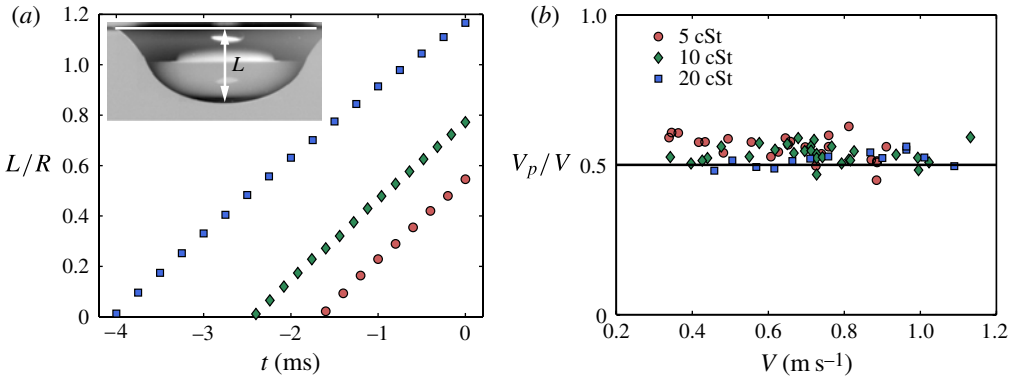

FIGURE 2. (*a*) Penetration depth L normalized by the drop radius R as a function of time of impact of droplets of the same impact velocity ($V = 0.55$ m s^{-1}) but different viscosities as shown in the legend. The rupture time of the air film is taken as the reference time ($t = 0$). (*b*) Normalized penetration velocity V_p/V for various impact velocities and viscosities.

the penetration velocity is found to be weakly dependent on the liquid viscosity (up to the maximum viscosity used in our experiment) and about $V_p \approx V/2$. This penetration velocity can be understood from an energy argument. First, let us consider a liquid volume Ω at the bottom of the drop. This volume has the shape of a spherical cap and velocity V. Thus, the initial kinetic energy of Ω before impact is $E^0_\Omega = \rho_l \Omega V^2/2$. The same volume of liquid at a small time t after the impact time is then assumed to have velocity V_p and takes the shape of a hemisphere of radius R_p, i.e. $\Omega = 2\pi R_p^3/3$. The kinetic energy of Ω at t is $E^t_\Omega \approx \rho_l \Omega V_p^2/2$. Assuming that the velocity field in the pool at time t is approximately a radial flow field with a point source at the centre of the hemisphere, we may estimate the kinetic energy of the liquid in the pool at time t as $E^t_P \approx \pi \rho_l R_p^3 V_p^2 = 3\rho_l \Omega V_p^2/2$. From the conservation of energy, $E^0_\Omega = E^t_\Omega + E^t_P$, we indeed obtain $V_p \approx V/2$. Note that this result can alternatively be obtained by using conservation of momentum and has been known in the context of penetration mechanics (see e.g. Birkhoff *et al.* 1948; Yarin, Rubin & Roisman 1995). From this model, we also infer that it is possible to change the penetration velocity by using liquids of different densities for the drop and for the pool. This speculation, however, is beyond the scope of the present study and needs further experimental verification.

3.2. *Thinning of air film*

If figure 3(*a*), we show several profiles of the air film thickness of experiments with the same impact conditions ($\nu_l = 20$ cSt and $V = 0.5$ m s^{-1}); each profile is extracted from an interference fringe obtained at a distinct focusing distance D_c (see figure 1*b*). This allows us to reconstruct the change in the air thickness profile as it moves into the liquid pool. Here we assume that the air thickness profile at a fixed distance under the pool's surface does not change for repeated experiments with the same impact conditions since the impact dynamics are highly reproducible. Indeed, we have verified the good reproducibility (using side-view recording) of the experiments. In particular, it takes the same time interval after the impact time for the film to rupture. As a result, repetition of the experiment with varying D_c provides the evolution of the thickness profile at the bottom of the air film.

https://doi.org/10.1017/jfm.2013.261 Published online by Cambridge University Press

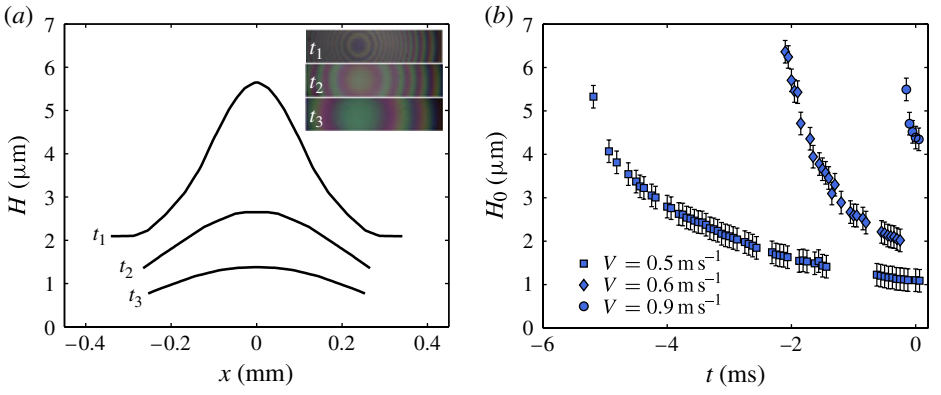

FIGURE 3. (*a*) Air film profile measured at different times of impact of 20 cSt droplets. The impact velocity is $V = 0.5$ m s^{-1}, $t_1 = -4.9$ ms, $t_2 = -2.8$ ms, $t_3 = -0.7$ ms. (*b*) Air film thickness at the bottom of the film ($H_0 = H(x = 0)$) as a function of time t for the impact of 20 cSt droplets at different impact velocities. The reference time for both panels is the rupture time.

In figure 3(*b*), we show the thickness evolution at the bottom of the air film $H_0 = H(x = 0)$ for impact of 20 cSt droplets on a liquid pool at three different velocities $V = 0.5$, 0.6 and 0.9 m s^{-1}. The plot shows that the dynamic of the air film is extremely sensitive to the impact velocity: increasing V from 0.5 to 0.9 m s^{-1} decreases the rupture time of the air film from 5.2 to 0.15 ms. We also observe that the air film thickness is much higher at the rupture time ($t = 0$ ms) for impact at larger V, as the air trapped at the bottom of the air film does not have time to drain out.

3.3. *Rupture of air film*

To characterize the rupture dynamics, we measure the arclength S between the bottom of the air film and the initial rupture position for the different viscosities (5, 10, 20 cSt) and impact velocities (from 0.3 to 1.8 m s^{-1}). In figure 4, we show a plot of S versus V. The plot consists of three separate datasets corresponding to three viscosities. It shows that S decreases with either increasing velocity or decreasing viscosity. Moreover, varying the viscosity only shifts the $\log_{10}S$ versus $\log_{10}V$ curve, suggesting that the data can be collapsed onto a master curve.

In order to explain the observed result for the rupture position, we first propose a mechanism for film rupture. We first note that the air layer thickness decreases radially outwards, as suggested by the measured thickness profiles at the bottom of the air film (figure 3*a*). On the other hand, since the air thickness close to the free surface is also large, we infer that there is a radial position where the film thickness is smallest and, as a result, the air film is most likely to collapse here. This radial position can be determined experimentally by measuring the arclength S to the bottom of the air film (see figure 4 for definition). Note that, once the film thickness is smaller than a critical value, which is of the order of 100 nm, the van der Waals force between the two surfaces of the film will become dominant and rupture the film immediately (see Couder *et al.* 2005; Dorbolo *et al.* 2005; Thoroddsen *et al.* 2012).

We now seek to derive the dependence of S on the liquid viscosity, the drop radius R and the impact velocity V. The liquid and gas have densities ρ_l and ρ_g, and kinematic viscosities ν_l and ν_g, respectively. The film thickness is denoted by h. The air flows out of the layer with velocity u_g due to the pressure excess ΔP. Since the

https://doi.org/10.1017/jfm.2013.261 Published online by Cambridge University Press

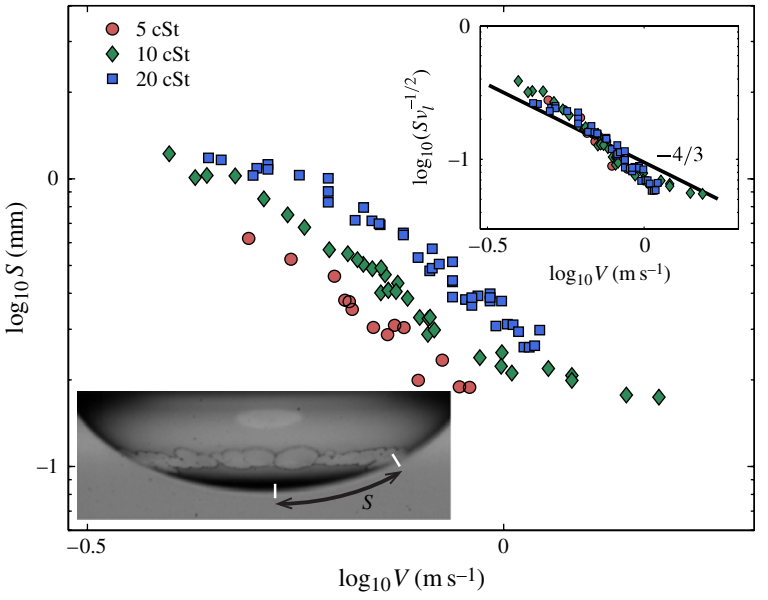

FIGURE 4. Log–log plot of the rupture position S as a function of impact velocity for different viscosities. Inset: log–log plot of $S\nu_l^{-1/2}$ as a function of impact velocity. The solid line represents the exponent $-4/3$ of the scaling law (3.5).

impact velocity is relatively low, we take the hydrostatic pressure $\Delta P \sim \rho_l g R$, where g is the gravitational acceleration. Because S was shown to depend on the liquid viscosity, we cannot treat the liquid–air interfaces as rigid surfaces. Instead, we assume continuity of the shear stress across the interface. Hence, the shear stress in the gas layer, $\tau_g \sim \rho_g \nu_g u_g / h$, is balanced with the shear stress in the liquid, $\tau_l \sim \rho_l \nu_l u_g / \delta$, where $\delta \sim \sqrt{\nu_l S / u_g}$ is the thickness of the boundary layer in the liquid. This gives us an estimate for the gas velocity:

$$u_g \sim \frac{\rho_g^2}{\rho_l^2} \frac{\nu_g^2 S}{\nu_l h^2}. \tag{3.1}$$

Typically, $S \approx 1$ mm and $h \approx 1$ μm in our experiments. From these values, (3.1) gives us the estimate for the gas velocity $u_g \approx 4$ cm s^{-1}. This is comparable to the velocity of gas exiting the gap between an impacting droplet and a solid surface measured in van der Veen *et al.* (2012).

Next, for the gas flow in the gap, we assume the lubrication approximation:

$$\frac{\Delta P}{S} \sim \rho_g \nu_g \frac{u_g}{h^2}. \tag{3.2}$$

To estimate h, we use the initial air gap at the impact time, which is similar to the initial air gap for impact on a solid surface (Bouwhuis *et al.* 2012):

$$h \sim R \left(\frac{\rho_g \nu_g}{\rho_l V R} \right)^{2/3}. \tag{3.3}$$

https://doi.org/10.1017/jfm.2013.261 Published online by Cambridge University Press

From (3.1)–(3.3), we obtain S as a function of V and ν_l:

$$S \sim \left(\frac{\rho_l}{\rho_g \nu_g}\right)^{1/6} g^{1/2} R^{7/6} \nu_l^{1/2} V^{-4/3}. \tag{3.4}$$

As we only varied the viscosity and the impact velocity in our experiment, the above expression can be written as

$$S \sim \beta \nu_l^{1/2} V^{-4/3}, \tag{3.5}$$

where the prefactor β is a dimensional constant. In the inset of figure 4, we show a log–log plot of $S\nu_l^{-1/2}$ versus V. Although the impact velocity in our experiments only spans a limited range, the data collapse onto a single master curve suggests that the model reasonably predicts the dependence of S on the liquid viscosity. Nonetheless, $S\nu_l^{-1/2}$ displays a slightly stronger dependence on V than is predicted by the scaling law (3.5). We attribute this slight deviation to the curvature of the air film, while our model was derived for a flat air film.

3.4. *Bubble entrapment*

After the air film ruptures, the entrained air contracts towards the bottom to create one or several primary bubbles and leaves behind those that are much smaller in size. This air entrainment process is often referred to as Mesler entrainment (see Esmailizadeh & Mesler 1986; Pumphrey & Elmore 1990). If the impact velocity is small, the volume of the small bubbles left behind may be comparable to that of the primary ones. In our experiment, this happens for $V < 0.5$ m s^{-1} for all three silicone oils. However, for higher impact velocity, the volume of the primary bubbles Ω_b is dominant and can be used to estimate the total volume of the entrapped air. Here, we focus on the latter case and measure Ω_b with varying viscosity and impact velocity (0.5 m s^{-1} $< V <$ 2.3 m s^{-1}). We also relate the entrapped air volume here to other situations where bubble entrapment is observed, namely impact of droplets on solid surfaces (see e.g. Chandra & Avedisian 1991; Thoroddsen & Sakakibara 1998; van Dam & Le Clerc 2004; Thoroddsen *et al.* 2005; van der Veen *et al.* 2012), and impact of solid spheres on liquid surfaces (Marston, Vakarelski & Thoroddsen 2011). In figure 5, we show the entrapped bubble volume obtained in three different cases: silicone oil droplets impacting oil surfaces (present study), ethanol droplets impacting solid surfaces (Bouwhuis *et al.* 2012), and solid spheres impacting liquid surfaces (Marston *et al.* 2011). The solid line represents the scaling law that was derived theoretically (see Hicks & Purvis 2010, 2011; Bouwhuis *et al.* 2012) and supported experimentally (Bouwhuis *et al.* 2012):

$$\frac{\Omega_b}{\Omega_d} \sim St^{-4/3}, \tag{3.6}$$

where $\Omega_d = 4\pi R^3/3$ and $St = \rho_l RV/\rho_g \nu_g$ are the volume and the Stokes number of the drop, respectively. In the case of solid spheres impacting on liquid surfaces, the Stokes number is defined as $St_s = \rho_s R_s V_s/\rho_g \nu_g$, where ρ_s, R_s and V_s are the density, radius and impact velocity of the solid spheres, respectively. Both datasets for impact of ethanol droplets on solid surfaces and for impact of solid spheres on liquid surfaces collapse onto the solid line that represents the scaling law (3.6). On the other hand, the data for the impact of droplets on liquid surfaces appear to have the same scaling exponent but are shifted towards higher Stokes number.

https://doi.org/10.1017/jfm.2013.261 Published online by Cambridge University Press

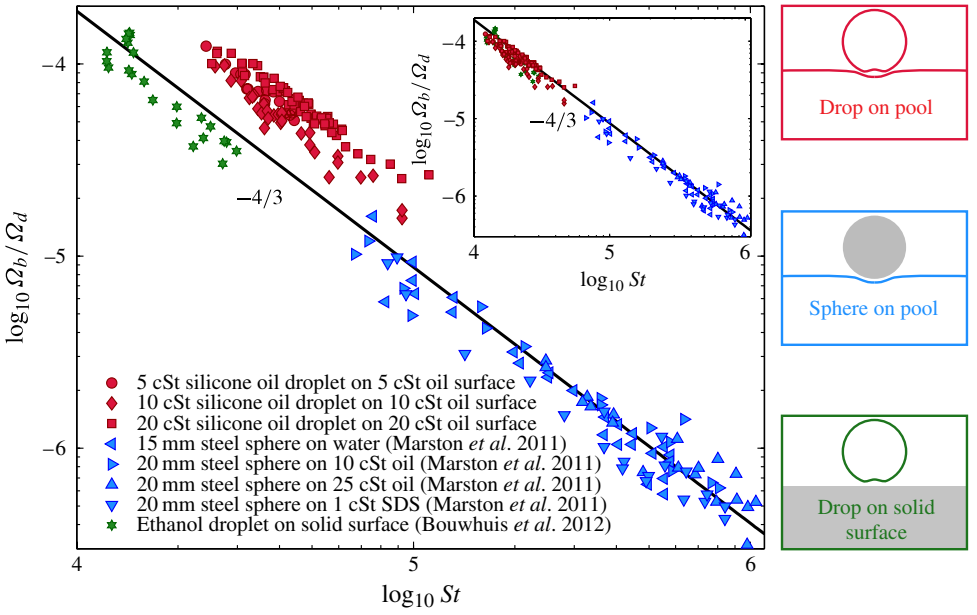

FIGURE 5. Log–log plot of the normalized bubble volume Ω_b/Ω_d as a function of Stokes number in three cases sketched on the right-hand side: impact of droplets on liquid surfaces (present study); impact of solid spheres on liquid surfaces (Marston *et al.* 2011) (SDS = sodium dodecyl sulfate); and impact of droplets on solid surfaces (Bouwhuis *et al.* 2012). The solid line represents the $-4/3$ scaling law presented in (3.6). Inset: collapse of the dataset for impact of droplets on liquid surfaces on other datasets after using the Stokes number calculated using the penetration velocity of the air film layer.

To understand this result, let us first consider the impact of droplets on liquid surfaces. In this case, the two approaching surfaces (of the droplet and the liquid pool) are both deformable; the air film penetrates into the liquid pool with velocity $V_p \approx V/2$. In contrast, for the impact of solid spheres on liquid surfaces, or the impact of droplets on solid surfaces, only one of the approaching surfaces is deformable. In these cases, the air film moves into the liquid bulk with the impact velocity. This observation prompts us to use V_p instead of V as the relevant velocity to calculate the Stokes number for the case of two deformable surfaces. In the inset of figure 5, we show the bubble volume for all cases, with the modified Stokes number $St = \rho_l R V_p/\rho_g \nu_g$ for the case of droplets impacting liquid pools. The dataset for impacts of droplets on liquid surfaces indeed now collapses onto the same line as the other two sets of data and is consistent with the scaling law (3.6). Note that the solid surfaces for all of these datasets are hydrophilic. In the case that the solid surfaces are hydrophobic, it is possible that the normalized bubble volume depends differently on the Stokes number, as the air entrapment mechanism may be different. This has not been tested, but is deduced from the related experiments by Duez *et al.* (2007) in which the splash occurrence is influenced by the wettability of the surface.

4. Conclusions

We have described the impact dynamics, including the penetration velocity V_p of the air film entrapped between the drop and the pool surface. We showed that V_p is

https://doi.org/10.1017/jfm.2013.261 Published online by Cambridge University Press

insensitive to the viscosity (from 5 to 20 cSt) and can be approximated as half of the impact velocity if the densities of the drop liquid and the liquid in the pool are comparable. This approximation is used to relate the volume of the entrapped bubble in this case to other cases such as the impact of droplets on solid surfaces and the impact of solid spheres on liquid surfaces. To this end, we have shown that the volume of the entrapped bubble is consistent with the scaling $\Omega_b/\Omega_d \sim St^{-4/3}$.

The dynamics of the air film entrapped under the droplets has also been studied in detail. We have measured the thickness profiles of the air film at different vertical locations using colour interferometry. From these measurements, the evolution of the film thickness at the bottom of the film was obtained for various impact velocities. The measured thickness evolution confirms that the air film gets thinner and thinner as a result of the air being drained out from the film. The draining process of the air eventually leads to the rupture of the film. We showed experimentally that the rupture position depends on both the liquid viscosity and the impact velocity. We also derived a scaling law of the rupture position taking into account the air flow in the film. This scaling law is qualitatively consistent with our experimental results.

Acknowledgements

This study was financially supported by the Foundation for Fundamental Research on Matter (FOM) and the European Research Council (ERC). The authors would like to acknowledge C. Clanet and D. Quéré for useful discussions. H. M. was supported by a scholarship in the framework of the Materials Science and Active Surface programme at École Polytechnique, Palaiseau, France (Chaire X-ESPCI-Saint Gobain).

References

Birkhoff, G., MacDougall, D. P., Pugh, E. M. & Taylor, G. 1948 Explosives with lined cavities. *J. Appl. Phys.* **19** (6), 563–582.

Bisighini, A., Cossali, G. E., Tropea, C. & Roisman, I. V. 2010 Crater evolution after the impact of a drop onto a semi-infinite liquid target. *Phys. Rev.* E **82**, 036319.

Bouwhuis, W., van der Veen, R. C. A., Tran, T., Keij, D. L., Winkels, K. G., Peters, I. R., van der Meer, D., Sun, C., Snoeijer, J. H. & Lohse, D. 2012 Maximal air bubble entrainment at liquid drop impact. *Phys. Rev. Lett.* **109**, 264501.

Chandra, S. & Avedisian, C. T. 1991 On the collision of a droplet with a solid surface. *Proc. R. Soc. Lond.* A **432**, 13–41.

Couder, Y., Fort, E., Gautier, C. H. & Boudaoud, A. 2005 From bouncing to floating: noncoalescence of drops on a fluid bath. *Phys. Rev. Lett.* **94**, 177801.

van Dam, D. B. & Le Clerc, C. 2004 Experimental study of the impact of an ink-jet printed droplet on a solid substrate. *Phys. Fluids* **16**, 3403–3414.

Deng, Q., Anilkumar, A. V. & Wang, T. G. 2010 The role of viscosity and surface tension in bubble entrapment during drop impact onto a deep liquid pool. *J. Fluid Mech.* **578**, 119–138.

Dorbolo, S., Reyssat, E., Vandewalle, N. & Quéré, D. 2005 Aging of an antibubble. *Eur. Phys. Lett.* **69**, 966–970.

Duchemin, L. & Josserand, C. 2011 Curvature singularity and film-skating during drop impact. *Phys. Fluids* **23**, 091701.

Duez, C., Christophe, Y., Clanet, C. & Bocquet, L. 2007 Making a splash with water repellency. *Nat. Phys.* **3** (3), 180–183.

Engel, O. G. 1967 Initial pressure, initial flow velocity, and the time dependence of crater depth in fluid impacts. *J. Appl. Phys.* **38** (10), 3935–3940.

https://doi.org/10.1017/jfm.2013.261 Published online by Cambridge University Press

ESMAILIZADEH, L. & MESLER, R. 1986 Bubble entrainment with drops. *J. Colloid Interface Sci.* **110** (2), 561–574.

HICKS, P. D., ERMANYUK, E. V., GAVRILOV, N. V. & PURVIS, R. 2012 Air trapping at impact of a rigid sphere onto a liquid. *J. Fluid Mech.* **695**, 310–320.

HICKS, P. D. & PURVIS, R. 2010 Air cushioning and bubble entrapment in three-dimensional droplet impacts. *J. Fluid Mech.* **649**, 135–163.

HICKS, P. D. & PURVIS, R. 2011 Air cushioning in droplet impacts with liquid layers and other droplets. *Phys. Fluids* **23**, 062104.

KOLINSKI, J. M., RUBINSTEIN, S. M., MANDRE, S., BRENNER, M. P., WEITZ, D. A. & MAHADEVAN, L. 2012 Skating on a film of air: drops impacting on a surface. *Phys. Rev. Lett.* **108** (7), 074503.

LEE, J. S., WEON, B. M., JE, J. H. & FEZZAA, K. 2012 How does an air film evolve into a bubble during drop impact? *Phys. Rev. Lett.* **109** (20), 204501.

LIU, Y., TAN, P. & XU, L. 2013 Compressible air entrapment in high-speed drop impacts on solid surfaces. *J. Fluid Mech.* **716**, doi:10.1017/jfm.2012.583.

MANDRE, S. & BRENNER, M. P. 2012 The mechanism of a splash on a dry solid surface. *J. Fluid Mech.* **690**, 148–172.

MANDRE, S., MANI, M. & BRENNER, M. P. 2009 Precursors to splashing of liquid droplets on a solid surface. *Phys. Rev. Lett.* **102** (13), 134502.

MANI, M., MANDRE, S. & BRENNER, M. P. 2010 Events before droplet splashing on a solid surface. *J. Fluid Mech.* **647**, 163–185.

MARSTON, J. O., VAKARELSKI, I. U. & THORODDSEN, S. T. 2011 Bubble entrapment during sphere impact onto quiescent liquid surfaces. *J. Fluid Mech.* **680** (1), 660–670.

PROSPERETTI, A. & OGUZ, H. N. 1993 The impact of drops on liquid surfaces and the underwater noise of rain. *Annu. Rev. Fluid Mech.* **25** (1), 577–602.

PUMPHREY, H. C., CRUM, L. A. & BJØRNØ, L. 1989 Underwater sound produced by individual drop impacts and rainfall. *J. Acoust. Soc. Am.* **85**, 1518–1526.

PUMPHREY, H. C. & ELMORE, P. A. 1990 Entrainment of bubbles by drop impacts. *J. Fluid Mech.* **220**, 539–567.

REIN, M. 1993 Phenomena of liquid drop impact on solid and liquid surfaces. *Fluid Dyn. Res.* **12** (2), 61–93.

SAYLOR, J. & BOUNDS, G. D. 2012 Experimental study of the role of the Weber and capillary numbers on Mesler entrainment. *AIChE J.* **58** (12), 3841–3851.

THORODDSEN, S. T., ETOH, T. G. & TAKEHARA, K. 2003 Air entrapment under an impacting drop. *J. Fluid Mech.* **478**, 125–134.

THORODDSEN, S. T., ETOH, T. G., TAKEHARA, K., OOTSUKA, N. & HATSUKI, Y. 2005 The air bubble entrapped under a drop impacting on a solid surface. *J. Fluid Mech.* **545**, 203–212.

THORODDSEN, S. T. & SAKAKIBARA, J. 1998 Evolution of the fingering pattern of an impacting drop. *Phys. Fluids* **10**, 1359–1374.

THORODDSEN, S. T., THORAVAL, M. J., TAKEHARA, K. & ETOH, T. G. 2012 Micro-bubble morphologies following drop impacts onto a pool surface. *J. Fluid Mech.* **708**, 469–479.

TRAN, T., STAAT, H. J. J., PROSPERETTI, A., SUN, C. & LOHSE, D. 2012 Drop impact on superheated surfaces. *Phys. Rev. Lett.* **108** (3), 036101.

VAN DER VEEN, R. C. A., TRAN, T., LOHSE, D. & SUN, C. 2012 Direct measurements of air layer profiles under impacting droplets using high-speed color interferometry. *Phys. Rev.* E **85** (2), 026315.

WEISS, D. A. & YARIN, A. L. 1999 Single drop impact onto liquid films: neck distortion, jetting, tiny bubble entrainment, and crown formation. *J. Fluid Mech.* **385**, 229–254.

WORTHINGTON, A. M. 1908 *A Study of Splashes*. Longmans, Green.

XU, L., ZHANG, W. W. & NAGEL, S. R. 2005 Drop splashing on a dry smooth surface. *Phys. Rev. Lett.* **94** (18), 184505.

YARIN, A. L. 2006 Drop impact dynamics: splashing, spreading, receding, bouncing. *Annu. Rev. Fluid Mech.* **38**, 159–192.

YARIN, A. L., RUBIN, M. B. & ROISMAN, I. V. 1995 Penetration of a rigid projectile into an elastic–plastic target of finite thickness. *Intl J. Impact Engng* **16** (5), 801–831.

https://doi.org/10.1017/jfm.2013.261 Published online by Cambridge University Press